Numerical modelling of the Sydney Harbour Estuary, New South Wales: Lateral circulation and asymmetric vertical mixing

Ziyu Xiao[a,b,*], Xiao Hua Wang[a,b], Moninya Roughan[a,d,e], Daniel Harrison[c,e]

[a] *The Sino-Australian Research Centre for Coastal Management, UNSW Canberra, Canberra, ACT, 2600, Australia*
[b] *School of Physical-Environmental and Mathematical Sciences, UNSW Canberra, Canberra, ACT, 2600, Australia*
[c] *Ocean Technology Group, School of Geosciences, University of Sydney, NSW, 2006, Australia*
[d] *School of Mathematics, University of New South Wales, Sydney, NSW, Australia*
[e] *Sydney Institute of Marine Science, Mosman, NSW, Australia*

A R T I C L E   I N F O

A B S T R A C T

A fully calibrated three-dimensional hydrodynamic model of the Sydney Harbour Estuary was used to determine the dominant forcing of regulating estuarine circulation in a sinuous channel under conditions of low river discharge during dry weather. The system, characterized by stratified flood and mixed ebb during spring tides, and stratified flood and ebb during neap tides, was analysed using model results of current profiles, density field, eddy viscosity and gradient Richardson number at a mooring station and cross-channel transect. The magnitude and direction of lateral circulation was modulated in the flood-ebb and spring-neap cycles due to changes in the interactions between the tides and the complex geometry. During spring tides, a differential-advection-induced lateral baroclinic pressure gradient tends to drive the lateral circulation and stratifies the water column. When the along-estuary circulation is strong enough to break the stratification induced by the lateral baroclinic pressure gradient, centrifugal force works in concert with nonlinear advection establishing a classical two-layer helical flow across the channel. Channel bends also induce vertical mixing as a result of the overturning of the density fields. The lateral circulation redistributes the differential-advection-induced lateral shear of the along-estuary momentum and is transferred to either reinforce or cancel the along-estuary circulation. The lateral bathymetry variability in a channel is therefore the key factor causing the intratidal asymmetries in the along-estuary circulations. Stratification suppresses lateral circulation during neap tides, and generates a three-layer lateral circulation structure in the water column during stratified ebb.

1. Introduction

Lateral circulation (or secondary circulation) has been recognized as an important process for redistributing scalars and momentum across an estuary channel and impacting along-estuary circulation (Smith, 1976; Lerczak and Geyer, 2004). The spatial and temporal variabilities in the lateral circulation have wide implications for channel morphology, sediment transport and the ecological environment. Mechanisms driving lateral circulation have been investigated in a number of studies in tidally driven estuaries.

For instance, Nunes and Simpson (1985) and Lerczak and Geyer (2004) found lateral flows can be driven by lateral density gradients induced by differential advection of along-estuary density gradients. Cheng et al. (2009) demonstrated lateral flows can be caused by lateral density gradients which form due to differences in mixing across the channel between the shoal and thalweg. Chant and Wilson (1997), and

Chant (2002) showed lateral circulation may be caused by the curvature effect due to channel bends and headlands. The role of Coriolis forcing in producing lateral circulation was investigated by Ott et al. (2002) and Huijts et al. (2009). Lateral circulation caused by the interaction between barotropic tides and variations in cross channel bathymetry was addressed by Li and O'Donnell (1997), while Chen and Sanford (2008) studied the role of boundary mixing on a sloping bottom on lateral circulation. Given the complex geometry of estuarine channels, more than one mechanism can contribute to lateral circulation.

The study of centrifugal force and baroclinic pressure gradient interactions, and their potential impact on lateral circulation, including intra-tidal asymmetry, is the subject of numerous papers (Chant and Wilson, 1997; Seim and Gregg, 1997; Lacy and Monismith, 2001; Kim and Voulgaris, 2008; Buijsman and Ridderinkhof, 2008; Nidzieko et al., 2009; Becherer et al., 2015; Pein et al., 2018).

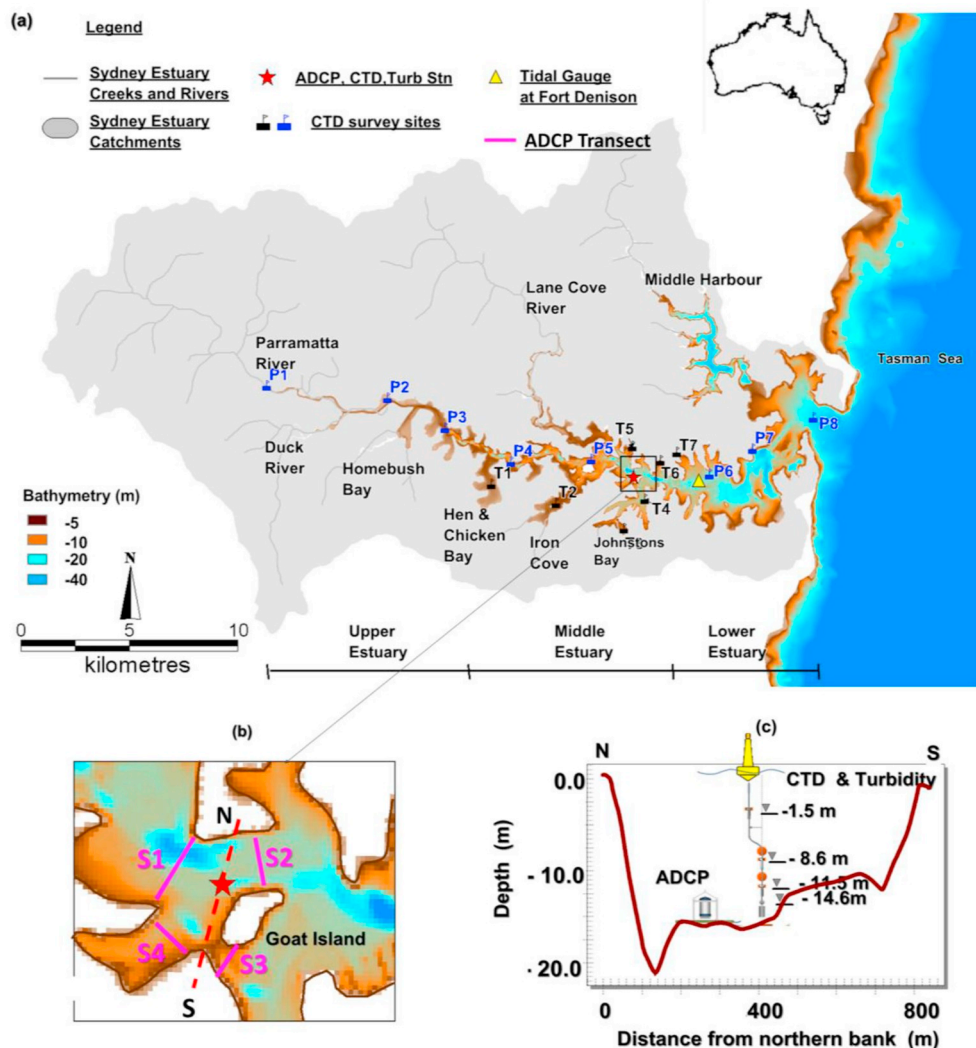Few studies however address the response of the vertical mixing to

Fig. 1. (a) Map of the Sydney Harbour Estuary. The colour scale shows the bathymetry grid. Indicated are the locations of the CTD surveys in the estuary tributaries and embayments (black flag, T1–T8), the axial CTD surveys (blue flag, P1–P8), the tidal gauge at Fort Denison (yellow triangle) and the ADCP, CTD, bottom turbidity mooring station near Goat Island (red star); **(b)** Magnified map of the mooring station near Goat Island (GI) with bathymetry shown by the colour; the ADCP transects (purple lines, S1−S4); **(c)** Setup of mooring station near Goat Island. (For interpretation of the references to colour in this figure legend, the reader is referred to the Web version of this article.)

lateral circulation caused by different forcings in channel bends. Blanckaert and de Vriend (2005a,b) conducted laboratory studies to investigate unstratified flows in sharply curved open channels, finding that turbulent kinetic energy was redistributed over the cross-section when compared to straight open channels. They found that, similar to buoyancy, channel curvature supressed turbulent activity, and stimulated wave-like mean flow. Seim and Gregg (1997) used the Froude Number (F_r) to evaluate the relative importance of vertical stratification and centrifugal force in Tacoma Narrows, where secondary circulation was found to be responsible for overturning the density field and inducing vertical mixing. Pein et al. (2018) found meanders reduced along-estuary flows during flood via friction, causing stronger vertical mixing; during ebb, stratification suppressed friction and lateral flows developed.

Because lateral circulation redistributes along-estuary momentum, lateral circulation could be as important for estuarine circulation as the along-channel gravitational circulation (Lerczak and Geyer, 2004). Asymmetric lateral circulation was found to induce asymmetric along-estuary circulation which resulted in a tidally averaged exchange flow (Becherer et al., 2015). Apart from using the along-channel and cross-channel momentum balance to analyse the interactions between the various driving forces, many recent studies have adopted the vorticity equation to study the generation and interplay of lateral and longitudinal circulations (Li et al., 2012; Collignon and Stacey, 2012; Becherer et al., 2015). Both methods included terms representing the Coriolis force, centrifugal force, baroclinic pressure gradient, frictional dissipation and non-linear advection.

In this paper, we extend upon previous studies of estuarine circulation in the Sydney Harbour Estuary (SHE), Australia. Continuous estuarine exchange with tidal mixing during low river inflow prevails in the SHE and makes a great contribution to the import and export of materials (Das et al., 2000). Under high river flow conditions, the estuary experiences strong stratification (Lee et al., 2011; Lee and Birch, 2012). In this study we use a combination of monitoring and modelling to address unanswered questions, including how the estuarine circulation is influenced by the interaction between tides, complex channel bends and irregular bathymetry during low river flow conditions, and how lateral flows in a channel bend impacts mixing behaviour and feedback in estuarine circulation during the different tidal phases. This is the first study to analyse the SHE dynamics using a high resolution 3D unstructured model in baroclinic mode, encompassing the river system, estuary, extending onto the continental shelf and is consequently the first to represent the full river-estuary-coastal continuum. It demonstrates that the circulation and mixing in a geometrically complex system with low river flow are more complicated than previously thought, and shows that bathymetry and model resolution are important when trying to resolve these systems.

This paper is organized as follow. Section 2 describes the study site, field observation, model configuration and equations used to define stratification stability. The model was calibrated against field survey data in Section 3. The intratidal and spring-neap cycles in water level, current velocity, density, eddy viscosity and mixing at the mooring

station and across the estuarine channel is shown in Section 4.1 and 4.2. In Section 4.3, the effect of asymmetric lateral circulation on long-itudinal circulation was investigated using an along-channel vorticity budget. The cross-channel momentum was analysed in Section 4.5. In Section 4.6, lateral momentum analysis was applied over the whole estuary.

2. Methods

2.1. Study site

The Sydney Harbour Estuary, a drowned river valley (Roy, 1983), receives river discharge from a highly urbanised (77%) catchment ($\sim 480 \, km^2$) which drains into the Tasman Sea on the east coast of New South Wales, Australia (Fig. 1). The estuary's wide mouth ($\sim 3 \, km$ wide) allows tides to propagate throughout the entire system, approximately 30 km from mouth to headwaters. Tides are semi-diurnal with a maximum tidal range of 2.1 m, a mean spring range of 1.3 m and a mean neap range of 0.8 m at Fort Denison (FD; Fig. 1), 8 km from the mouth of the estuary. Features of the waterway include a complex shoreline, meandering main channel, varying bathymetry (average depth 13 m, maximum depth 46 m) and large regions of shallow off-channel embayments which contain a significant mass of tidal water and sediments. The estuary receives 60–90% of its freshwater from the Parramatta, Lane Cove and Duck Rivers following high precipitation events (Lee and Birch, 2012, Fig. 1). Estuarine water is well mixed by tides during prolonged periods of low rainfall ($< 5 \, mm/day$), and becomes stratified during occasional periods of high rainfall ($> 50 \, mm/day$) over a few days (Birch and Rochford, 2010; Hatje and Birch, 2001; Lee et al., 2011; Lee and Birch, 2012).

2.2. Field observation

Surface water elevations were obtained from the FD tidal gauge and the mooring station near Goat Island (GI), both recorded at a 60-min sampling interval. Hourly wind fields were extracted from Bureau of Meteorology (BOM) station at FD and converted into along- and cross-estuary wind velocity components (Fig. 4b). A bottom-mounted (up-ward-looking) acoustic doppler current profiler (ADCP) was deployed in 18 m of water in the middle of the main estuarine channel near GI (Fig. 1a and b), by Oceanographic Field Services Pty Ltd, Australia. The 1200 kHz ADCP had a vertical bin size of 0.5 m and measured from depths of 1.5 m–15.5 m. Measurements were limited at the surface and the bottom blank areas. Current speed and direction data were extracted for the model simulation period at 5-min time intervals. Data were then averaged hourly. Two 600 kHz ADCPs were operated in bottom-tracking mode to conduct transect profiling along four estuary cross-sections, on 4/12/2013, over a full flood-ebb cycle during a spring-tide cycle. The time lapse between consecutive measurements at each cross-section was approximately 15 min, and one round trip for the four sections was finished within 1 h (section locations are shown in Fig. 1b).

The CTD profiling system deployed at GI station consisted of three TRDI Citadel CTDs suspended vertically below the surface by mid-water floats and a bottom-mounted Seabird SBE37 (Fig. 1c). The sensors collected samples at depths of 1.3 m, 7.3 m, 10.6 m and 13.7 m at 5-min sampling intervals. Monthly shipboard survey was conducted in 2013 to collect vertical salinity measurements at ~ 20 sites (Fig. 1a; T1–T8; P1–P8). A CTD probe (YSI Model with a YSI 6136 optical turbidity probe) was lowered manually from the surface to the bottom at 2s re-cording intervals. Monthly CTD profiles measured across the whole estuary were used as input to generate initial condition for salinity in the model and to compare the predicted spatial salinity variations (see Appendix A for details).

2.3. Model description

An unstructured-grid, Finite-Volume, three-dimensional primitive-equation Coastal Ocean Model (FVCOM; Chen et al., 2003) was used to reproduce the coastal oceanic and estuarine circulation. FVCOM si-mulates water surface elevation, velocity, temperature and salinity by solving the equations of momentum, continuity, temperature, salinity and density in an integrated form to conserve mass. In addition, specific modules can be added to simulate sediment dynamics and water quality. A detailed description of the numerical algorithm is provided by Chen et al. (2003). The use of an unstructured triangular grid in the horizontal plane gives greater flexibility for areas with a complex coastline and allows for greater refinement of local grids in coastal areas, a suitable approach for the SHE. A sigma vertical coordinate is used to better represent the irregular bottom topography in the three-dimensional domain. The model uses the Smagorinsky (1963) and the modified Mellor-Yamada level 2.5 (Mellor and Yamada, 1982) turbu-lence closure schemes for horizontal and vertical mixing, respectively. The wetting/drying algorithm, which incorporates a bottom viscous layer of specified thickness ($D_{min} = 5 \, cm$ in this case), was applied to take into account the impact of tidal flats. Water depths at nodes and cells were checked against D_{min}, and if less than D_{min}, the velocity in the triangle cell and the flux at the cell boundaries were set to zero in calculating of volume flux to ensure mass conservation (Chen et al., 2003).

2.4. Model configuration

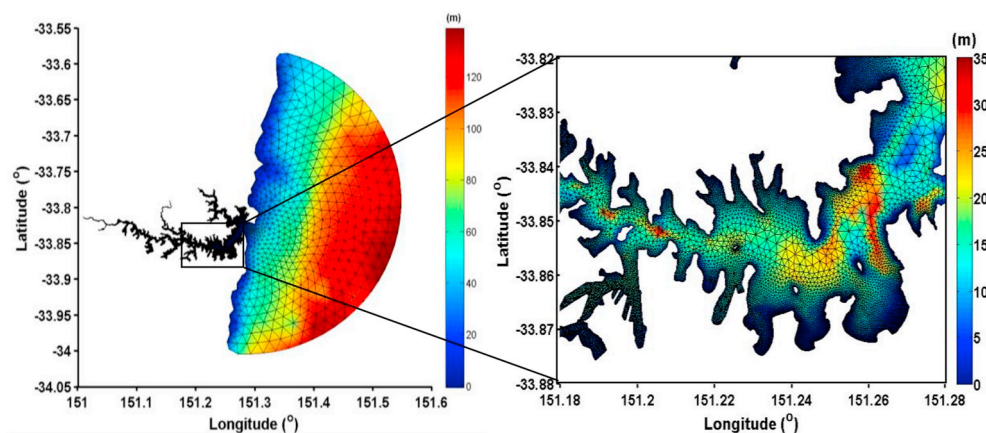The computational domain extended $\sim 23 \, km$ offshore to include

Fig. 2. Model domain for the Sydney Harbour Estuary. The unstructured triangular mesh varies from 30 m in the harbour to 2000 m at the ocean boundary. The model depth is indicated by the coloured shading.
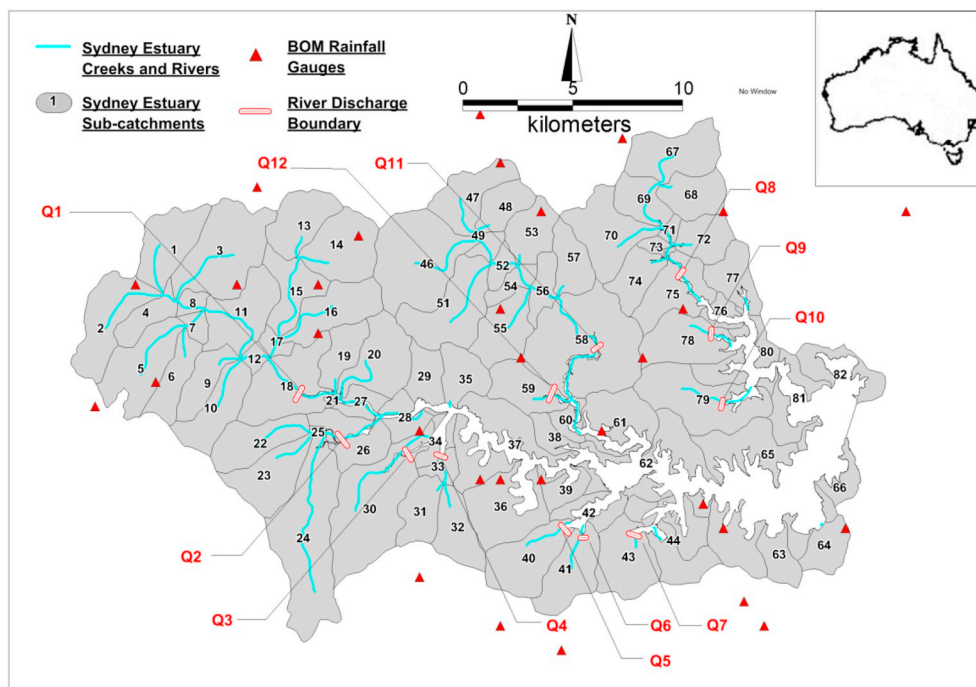
Fig. 3. Hydrology model WBNM (Watershed Bounded Network Model) used for rainfall-runoff estimation. The Sydney catchment is divided into 82 sub-catchments (labelled 1–82). The red lines (Q1−Q12) show the location of the freshwater inputs at the model boundary as edge sources. A total of 38 rainfall stations were used for rainfall pattern generation. (For interpretation of the references to colour in this figure legend, the reader is referred to the Web version of this article.)

the impact of East Australian Current intrusion on the estuarine circulation, and ∼30 km upstream westward to include freshwater discharge points (Fig. 2). The grid consisted of 79,278 elements (triangles) and 43,584 nodes (of the triangles), forming a mesh of triangles with variable cell width ranging from 2000 m at the open ocean boundary to 30 m in the estuary. The grid resolution is more accurate than current available 3D hydrodynamic model which is averagely 60 m grid cell size for the estuary (Lee and Birch, 2012). Over 50% of the cells were less than 50 m wide. The vertical resolution was 15 sigma layers, with a uniform thickness in the middle (11% of the total depth), and higher resolution near the surface and bottom (1% of the total depth) to resolve complex dynamics at surface and bottom. The bathymetry data were interpolated linearly to a spatial resolution of 30 m. Model coordinates were x as the along-estuary axis (positive eastward), y as the cross-estuary axis (positive northward) and z as the vertical axis (positive upward).

The model was spun up for one month and run for a further 1.5 month for the period 15/10/2013 to 31/12/2013, forced with tides and river discharge (Case 1). An additional model run applied river discharge only (Case 2). Output from two model runs were compared to examine the role of tidal/river interactions on mixing asymmetries. Finally, the model was driven by surface wind forcing, tides and freshwater inflow (Case 3) to examine the wind impact on vertical mixing. The model was initialized with a zero-velocity field, uniform water temperature of 25 °C and an initial horizontal salinity gradient based on the CTD survey conducted on 15/10/2013 (Fig. A-1). Salinity calibration was performed using the model spin up for one month to reach near-equilibrium state. Open-boundary conditions were specified by tidal elevations simulated using the TPXO7.2 global ocean tide model (http://volkov.oce.orst.edu/tides/global.html). The dataset consisted of four diurnal constituents, Q_1, O_1, P_1, K_1, four semi-diurnal constituents, M_2, S_2, N_2, K_2, two long-period components, MF, MM, and three shallow-water constituents, M_4, MS_4, MN_4. The amplitude and phase for each constituent were derived at each open-boundary node from the coarser global model by linear interpolation. Surface wind fields were obtained from the global atmospheric reanalysis model ECMWF (European Centre for Medium-Range Weather Forecasts: www.ecmwf.int/) product ERA-interim. The spatial resolution was 0.125° × 0.125°, with output every 6 h. The ECMWF wind data were compared with the wind fields observed at two land-based meteorological stations (at Fort Denison and Botany Bay) provided by the BOM. For a one-year period (2013), the ECMWF wind data gave correlation coefficients of 0.68 and 0.59, respectively, in magnitude, and 0.58 and 0.53 in direction with the observation at the two stations. Catchment rainfall-runoff processes were simulated and calibrated with a purpose-built GIS-based stormwater model called WBNM (Watershed Basin Network Model). Twelve major inflow locations were identified (not the origin of river discharge points, so the inflow salinity values are not equal to zero), labelled as Q1−Q12 in Fig. 3. The river discharge calibration was performed at the Q1 station, which is the main river discharging into the SHE. Freshwater inflow was added at the edge of model boundary elements, and the inflow salinity values are lack of sufficient monitoring following rainfall to address infrequent high precipitation conditions. By the fact that the estuary mostly experiences no-to-low flow, we focus on quiescent conditions (< 5 mm/day) to better understand circulation during normal conditions. The model is likely to represent the observed behaviour during most of the year.

2.5. Stratification stability

To characterise the relative strength of the density gradient in stably stratified shear flows, the gradient Richardson number (R_{ig}) was calculated using

$$R_{ig} = \frac{N^2}{[(\partial u/\partial z)^2 + (\partial v/\partial z)^2]} \quad (1)$$

where $N^2 = -(g/\rho_o)(\partial \rho/\partial z)$, g is the gravitational acceleration and ρ_o the seawater density (1025 kg m^{-3}). The spring-neap and flood-ebb variations in stratification at the mooring station were determined using observed and modelled velocity gradients and the buoyancy frequencies at different depths, then interpolated through the whole water column. For a stably stratified shear flow, $R_{ig} > 0.25$ or normalized as $\log_{10}(R_{ig}/0.25) > 0$; for well-mixed flow, $R_{ig} < 0.25$ or $\log_{10}(R_{ig}/0.25) < 0$ (Miles, 1961; Howard, 1961). However, R_{ig} is linearly related to the top-to-bottom salinity difference when tidal straining dominates the tidal evolution of stratification, which does not account for unstratified flow. An alternative scaling to Eq. (1) is the bulk internal Froude Number (Ferziger et al., 2002; Nidzieko et al., 2009):
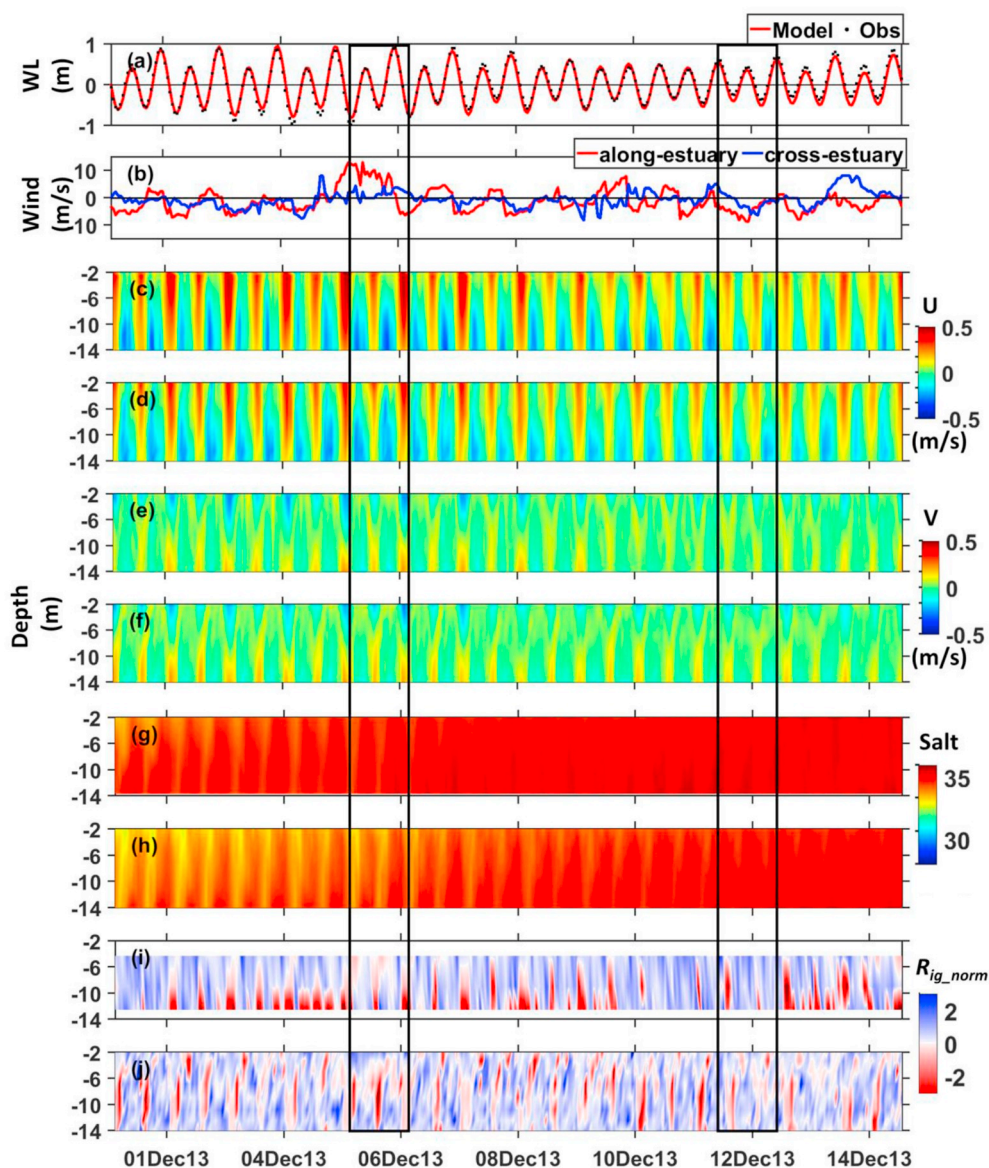
Fig. 4. Comparison of observations and model predictions at the Goat Island mooring station (location shown in Fig. 1b labelled with red star): (a) water level (m); (b) observed wind velocity components at Fort Denison (m/s); wind direction is rotated as along- and cross-estuary direction; positive value indicates down-estuary wind and cross-channel winds blowing from south to north; (c, d) along-estuary current velocity; (e, f) cross-estuary current velocity; (g, h) salinity; (i, j) normalized R_{ig}: positive values (blue) indicate stratification, negative values (red) indicate mixing. Black rectangles highlight selected spring and neap tidal cycle for analysis. (observed c, e, g, i; modelled d, f, h, j). (For interpretation of the references to colour in this figure legend, the reader is referred to the Web version of this article.)

Table 1

Comparison of the modelled and observed harmonic parameters for the main tidal constituents at the Fort Denison tidal gauge (FD) and the Goat Island ADCP station (GI).

Tidal Constituent	Amplitude (m)			Phase (°)		
	Observed	Model	Amplitude Deviation (%)	Observed	Model	Phase Deviation (°)
FD Q_1	0.02	0.02	−4.2	253.7	250.8	−2.8
GI Q_1	0.03	0.02	−30.1	40.9	24.1	−16.8
FD K_1	0.17	0.20	13.9	326.6	321.3	−5.3
GI K_1	0.18	0.21	14.4	283.1	285.1	2.0
FD O_1	0.10	0.10	−1.1	286.8	286.2	−0.6
GI O_1	0.10	0.10	12.8	358.4	1.87	3.47
FD N_2	0.12	0.11	−4.5	260.4	269.4	9.1
GI N_2	0.12	0.11	−11.0	22.7	20.7	−2.0
FD M_2	0.51	0.50	−2.2	278.2	277.6	−0.6
GI M_2	0.48	0.48	−0.1	341.1	343.4	2.3
FD S_2	0.13	0.12	−7.1	307.2	301.6	−5.6
GI S_2	0.10	0.10	−7.2	313.4	313.9	0.5

$$F_r = \frac{\bar{u}}{(N^2_{max}H)^{\frac{1}{2}}} \tag{2}$$

where is the total water depth, N_{max} the maximum buoyancy in the water column and $\bar{u}$ the mean flow. N_{max} provides a criterion for the condition of complete mixing when $F_r > 1$, which is similar to $R_{ig} < 0.25$ or $\log_{10}(R_{ig}/0.25) < 0$.

To determine when the centrifugal force is strong enough to overturn the density field downstream of the bend, the method applied by Seim and Gregg (1997) suggested the threshold causing well-mixed conditions:

$$\alpha F_r^2 \frac{B}{R_s} > 1 \tag{3}$$

where $\alpha = (u^2 - \bar{u}^2)/\bar{u}^2$ is a measure of vertical shear, B the channel width and R_s the radius of the bend.

3. Model validation

3.1. Tidal water levels

Hourly water elevations taken at GI station are compared with

Table 2
Model errors in the depth-averaged current velocities (m/s: along-estuary u, cross-estuary v) and bottom salinity at the mooring station.

	Mean error	RMS error	Skill Score	Correlation Coefficient
FD water level	−0.01	0.04	0.99	0.99
GI water level	−0.02	0.09	0.94	0.97
GI u	−0.03	0.05	0.84	0.95
GI v	0.01	0.03	0.52	0.71
GI salt	−0.21	0.42	0.20	0.68

model elevations in Fig. 4a (the elevations from the FD station showed similar results, and are not shown here). The model root-mean-square errors (RMSE) at the two sites were 0.04 m (0.2% of the water column depth) and 0.09 m (0.5% of the water column depth), respectively (Table 2). The skill scores (SS) was calculated as 0.99 at FD and 0.94 at GI; the correlation coefficients (CC) was estimated as 0.99 (FD) and 0.97 (GI; Table 2). A harmonic analysis was conducted using the T-Tide program in Matlab (Pawlowicz et al., 2002). The errors of amplitudes and phases of the six major tidal constituents (M_2, S_2, N_2, Q_1, K_1, O_1) are minor (Table 1). The amplitude and phase errors for M_2 were within 1 cm and 3° for the two stations.

3.2. Current velocity

Predicted current velocities showed close agreement with observed data (RMSE depth averaged velocity < = 0.05 m/s, mean error $u = -0.03$ m/s, mean error $v = +0.01$ m/s, Fig. 4c–f, 5c-f; Table 2). The errors are likely partly due to the coarse grid resolution in the complex curving flow channel, in which it is difficult to represent the bottom stress layer and the bathymetry variability accurately. Differences in the measurements averaged over a grid cell compared to the ADCP point measurement will further contribute separation between observation and predictions.

To accurately compare observed and modelled depth-averaged currents across the channel, for each ADCP transect, velocity observations were averaged over distance corresponding to model grid cell widths, with the comparisons shown in Fig. 6. Observed current velocities were typically larger than model velocities at all four transects (0.10 m/s < RMSE < 0.25 m/s). The difference may be associated with instrumental error, since the upper 2.5 m and lower 1.5 m of the water column is not captured by ADCP instruments. The way to calculate ADCP depth-averaged velocities was using snapshot values over the distance and comparing to the hourly averaged velocities from model at the corresponding grid cell, thus observed depth-averaged velocities may be artificially high.

3.3. Salinity and stratification

The salinity fluctuation trend was reproduced by the model but the fluctuation range was reduced compared to observation (Fig. 4g and h; Fig. 5g and h; Table 2). This discrepancy is likely partly due to over-estimation of vertical mixing by the model turbulence scheme (noting that salinity dominated density variations in this system), as indicated by normalized R_{ig} in Fig. 4i and j. Normalized R_{ig} indicated flood-ebb asymmetries in turbulent mixing during spring tide (Fig. 4i, first black boxed section). This behaviour was reasonably reproduced by the model (Fig. 4j, first black boxed section) however the model appears to generate intensified mixing relative to observations at other times.

The spatial precision of salinity dynamics was examined by the measured CTD profiles taken on 18/12/2013 under low-runoff conditions (Appendix Fig. A-2; survey sites are shown in Fig. 1a). Fig. 7 shows the observed and modelled along-estuary salinity gradients across the estuary during spring and neap tides. Overall, the validation indicated a reasonable calibrated hydrodynamic model in simulating tides and salinity dynamics for the study site near GI under quiescent

conditions (no-to-low rainfall).

4. Model results and discussion

4.1. Flood-ebb and spring-neap asymmetries

Vertical profiles of simulated along-estuary current velocity component (u), density field (rho), vertical eddy viscosity (K_m) and normalized R_{ig} at GI station during a full flood-ebb cycle over spring and neap are shown in Fig. 8. Overall, the estuary showed tidal cycles as mixed ebb and weakly stratified flood during spring, and stratified flood and ebb during neap. During spring tides, flood waters intruded into the estuary and induced weak stratification by differential advection processes. Saline waters were brought to the station via the bottom layer during flood, and the density increased vertically from bottom to top (Fig. 8e). Ebb waters mixed the freshwater from surface to bottom and changed the stratification until again a salt wedge flushed into the estuary during the next flood. The system became mixed during ebb tides (Fig. 8i). The maximum top-to-bottom density difference during spring tides was 1 kg/m³. Along-estuary currents were around 0.2 m/s weaker during flood than ebb (Fig. 8c). The vertical profile of the eddy viscosity (K_m) is used to indicate the intensity of turbulent mixing. The vertical eddy viscosity profiles demonstrate asymmetric turbulent mixing during the spring flood-ebb cycle (Fig. 8g). Maximum K_m (~0.04 m²/s) occurred at mid-depth (~10 m from the water surface) during periods of strong mixing by tides (Fig. 8g). Tidal mixing was suppressed by stratification during flood tides, coinciding with a lower K_m (~10^{-4} m²/s). The observed asymmetric stratification and vertical mixing differs from that associated with along-estuary tidal straining. This reversed asymmetry has a significant impact on salt and velocity transport in the estuary, and influences residual flows competing against gravitational circulation (Stacey et al., 2008). Similar behaviour has been observed in San Francisco Bay (Lacy et al., 2003) and the German Wadden Sea (Becherer et al., 2015), however this is the first record of this behaviour in the SHE.

In SHE, weaker tidal forcing during neap tides led to weaker along-estuary current velocities during flood and ebb tides (Fig. 8d), leading lateral density gradient to stratify the water column, with saline waters distributed from bottom-to-surface (Fig. 8f). The maximum top-to-bottom density difference during neap tide was 0.5 kg/m³ and the density field during neap is approximately 1 kg/m³ higher than during spring (Fig. 8f). A pulse of vertical turbulent mixing developed during neap ebb tides (Fig. 8h), but density stratification was preserved in the system. The K_m value observed was in the order of 10^{-4} m²/s (Fig. 8h), consistent with the persistent positive values of normalized R_{ig} throughout the water column associated with stratified systems (Fig. 8j).

The temporal variations in the river run-off, even small, may counteract the tidal inflow and have an impact on tidal effect and asymmetries. Constant negative values of normalized R_{ig} were only found within the top and bottom mixing layers when tidal forcing was ignored (Case 2; Fig. 8k and l). The no-to-low flow conditions and their eventual effects on estuarine circulation and asymmetries were not significant. The model does not replicate the behaviour of the system during moderate-to-high flow conditions when river runoff dominates estuary circulation; its influence requires further investigation.

Wind straining and mixing effect also plays an important role on estuarine circulation by down-estuary winds enhancing and up-estuary winds reducing vertical shear of density gradient (Scully et al., 2005). Normalized R_{ig} values in Case 3 (Figs. 8m,n) were compared to those in Case 1 (Fig. 8i and j) to examine the wind effects at GI station. Case 3 reproduced the flood-ebb asymmetry of vertical mixing as observed in Case 1 and introduced surface mixing caused by wind stress. Stratification during spring tide was enhanced by down-estuary winds on 05/12/2013 (wind speed up to 12 m/s; Fig. 4b), thus the ebb mixing observed in Case 1 (Fig. 8i) was partially suppressed by stratified water
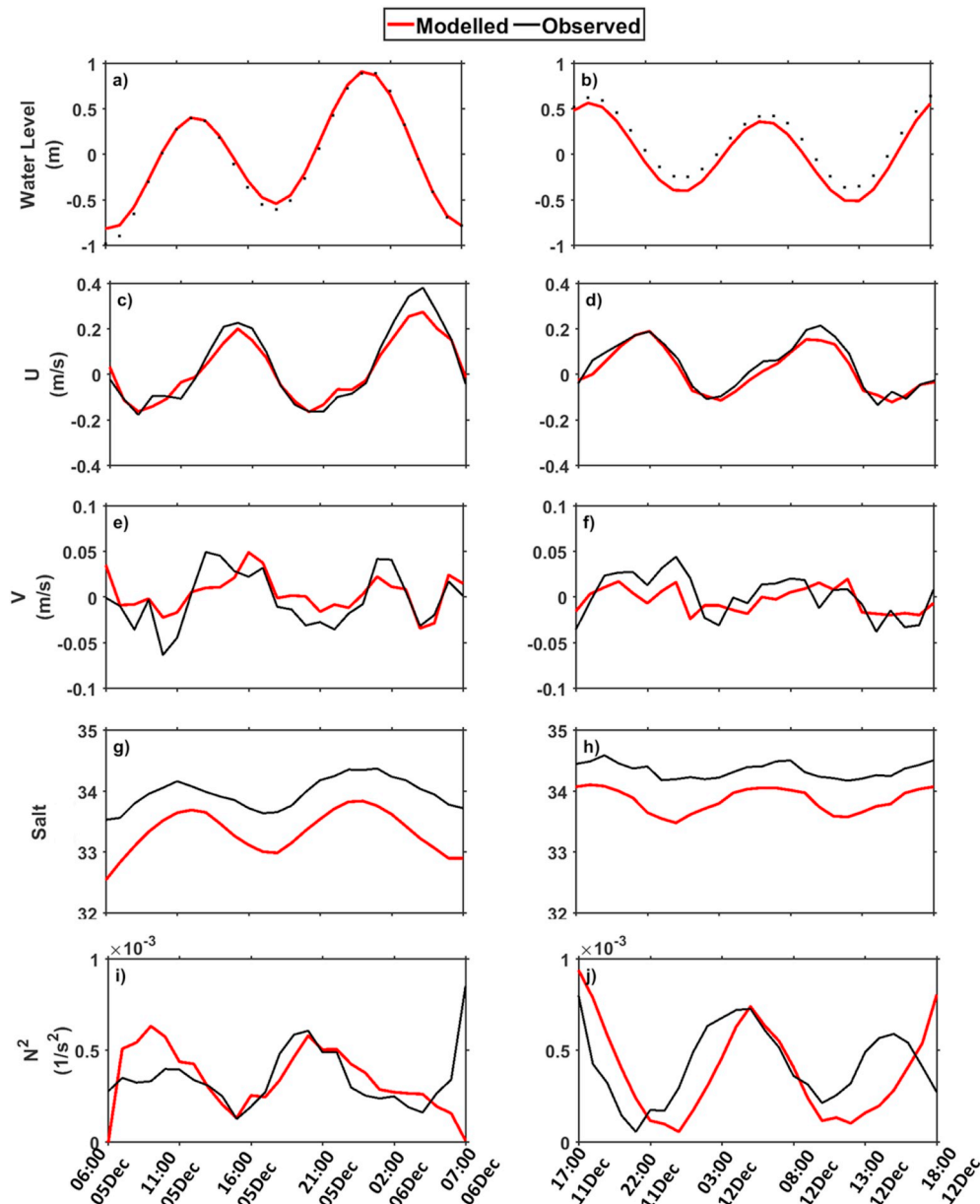
Fig. 5. Comparison of observed and modelled: (a, b) tidal elevation (m); (c, d) depth-averaged along-estuary current velocity; (e, f) depth-averaged cross-estuary current velocity; (g, h) bottom salinity; (i, j) buoyancy frequency at Goat Island during a spring (left) and neap (right) tidal cycle. Bottom salinity was obtained at a depth of 13.7 m. Buoyancy frequency (N^2) represents top-bottom stratification. Model red lines; observation black dots. (For interpretation of the references to colour in this figure legend, the reader is referred to the Web version of this article.)

column in Case 3 (Fig. 8m). Mixing during neap tides was enhanced by up-estuary winds on 12/12/2013 (wind speed up to 10 m/s), thus stimulating ebb mixing in Case 3 (Fig. 8n) which was not present in Case 1 (Fig. 8j). Wind forcing introduced additional straining or mixing effects on the system but does not explain the generation of flood-ebb asymmetry of vertical mixing which will be further investigated in Section 4.5.

4.2. Asymmetries in lateral circulation

Modelled lateral processes during flood and ebb over a spring-neap tidal cycle in Case 1 were studied across the channel near GI (Fig. 1b). The bathymetry across the channel is deep at the northern bank, with a shallow shoal near the southern bank. During spring tides, along-estuary currents were lowest over the shoal and highest over the thalweg (Fig. 9b, g). As a result, during flood tides, the lateral density gradient

coincided with differential advection forcing (Nunes and Simpson, 1985), with denser water on the thalweg and fresher water on the shoal (Fig. 9c). Advection of the along-estuary density set up lateral baroclinic pressure gradients driving anti-clockwise lateral circulation (facing down-estuary along the positive x axis), with cross-channel speeds reaching 0.1 m/s (Fig. 9a). During ebb, longitudinal currents were enhanced at the surface on the thalweg, with vertically sheared lateral currents reaching 0.2 m/s. Lateral flows exhibited temporal variability, in both magnitude and direction, with strong clockwise circulation during ebb and weak anti-clockwise circulation during flood (Fig. 9a, f). The lateral density gradient during ebb was more homogenous than during flood, with no large gradients at the surface and denser water remaining in the deep thalweg (Fig. 9h). This indicates that the lateral circulation during ebb was not dominated by the lateral baroclinic pressure gradient.

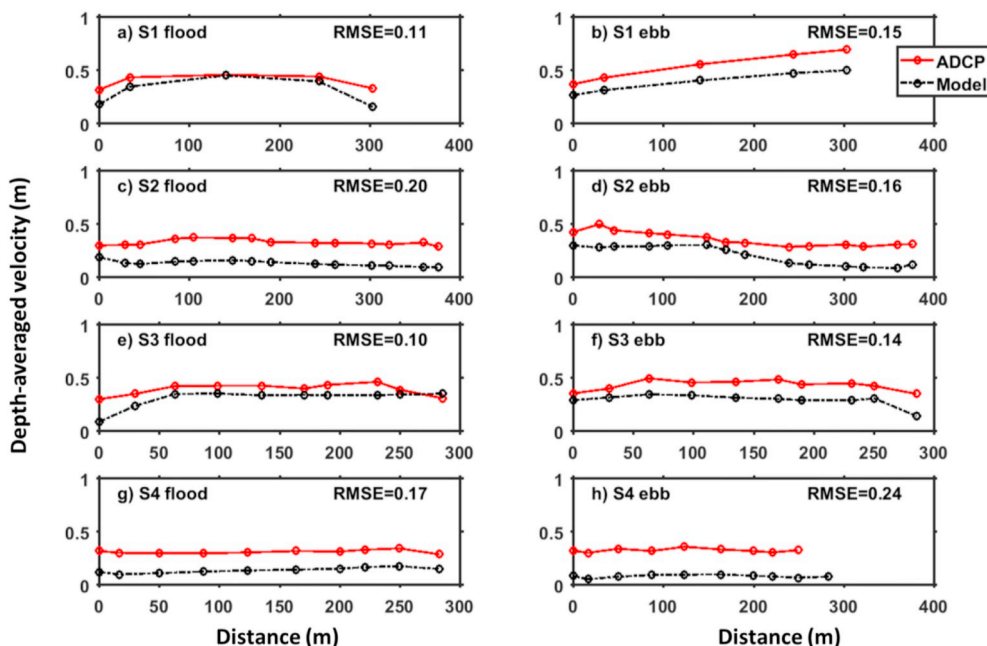During neap, lateral flows weakened (< 0.1 m/s) and the

Fig. 6. Comparison between measured and modelled depth-averaged velocities along S1—S4 during spring flood and ebb. ADCP transect locations are shown in Fig. 1.

circulation structure was influenced by stratification. During neap flood tides, density-driven circulation was present, with northward flow at the surface and southward flow at the bottom (Fig. 9k). A three-layer flow structure during neap ebb was observed as an anti-clockwise lateral circulation cell underneath a thin layer of southward flow at the surface (Fig. 9p). Williamson et al. (2012) reported a four-layer lateral circulation structure in an open channel around a 120° bend under stratification condition. In that study, the leading role switching between the baroclinic pressure gradient and centrifugal force over the different mixing layers was found to generate the complex circulation structure. Cheng et al. (2009) reported a four-layer transverse circulation during maximum ebb, driven by a lateral density gradient resulting from asymmetric vertical mixing between the thalweg and the shoal. The mechanisms driving the complex circulation pattern across the SHE channel and the reason for the observed flood-ebb asymmetries in lateral circulation are investigated using a lateral-momentum budget analysis in Section 4.5.

Wind forcing can also generate Ekman transport driving a counter-clockwise/clockwise lateral circulation under down-/up-estuary winds (looking into estuary) (Li and Li, 2012). The lateral circulation at GI station between Case 1 and Case 3 was examined (figure not shown here) and there is no great change of lateral circulation due to wind effects. The main channel in SHE is narrow (less than 2 km wide) which limits wind-induced lateral circulation to develop. Thus, lateral circulation in SHE is mainly driven by local forcing and have a weak lateral response to the along-estuary wind-forcing.

4.3. Lateral circulation feedback in the along-estuary circulation

The modelled depth-averaged along-estuary vorticity ω_x and the cross-estuary vorticity ω_y at the GI station were calculated in order to describe lateral and longitudinal circulation (Collignon and Stacey, 2012; Li and Li, 2012; Li et al., 2014). Both ω_x and ω_y demonstrate flood-ebb asymmetries, with a decrease during flood and increase during ebb (Fig. 10a and b). Similar fluctuation trends in ω_x and ω_y indicate that lateral circulation plays an important role in the
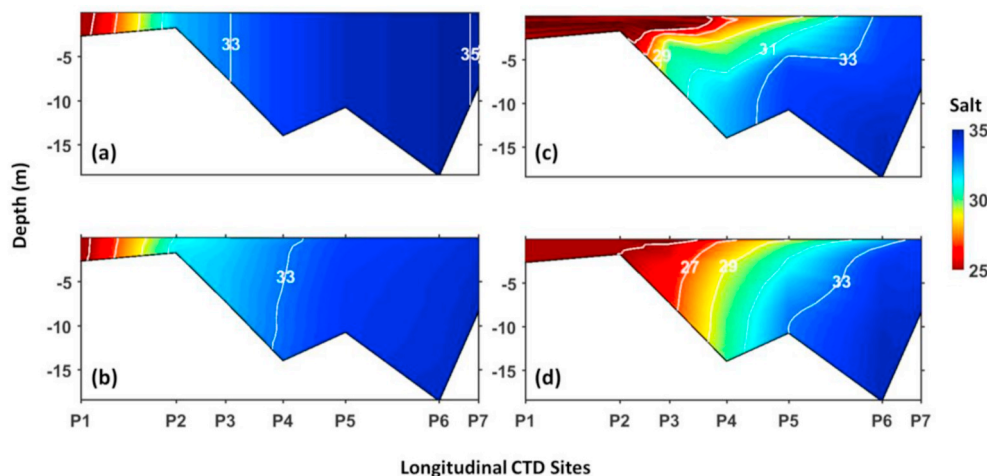

Fig. 7. Along-estuary distribution of salinity from axial CTD survey (a, c) in comparison with modelled salinity (b, d) during a period from flood to ebb over spring tide (left) and neap tide (right).
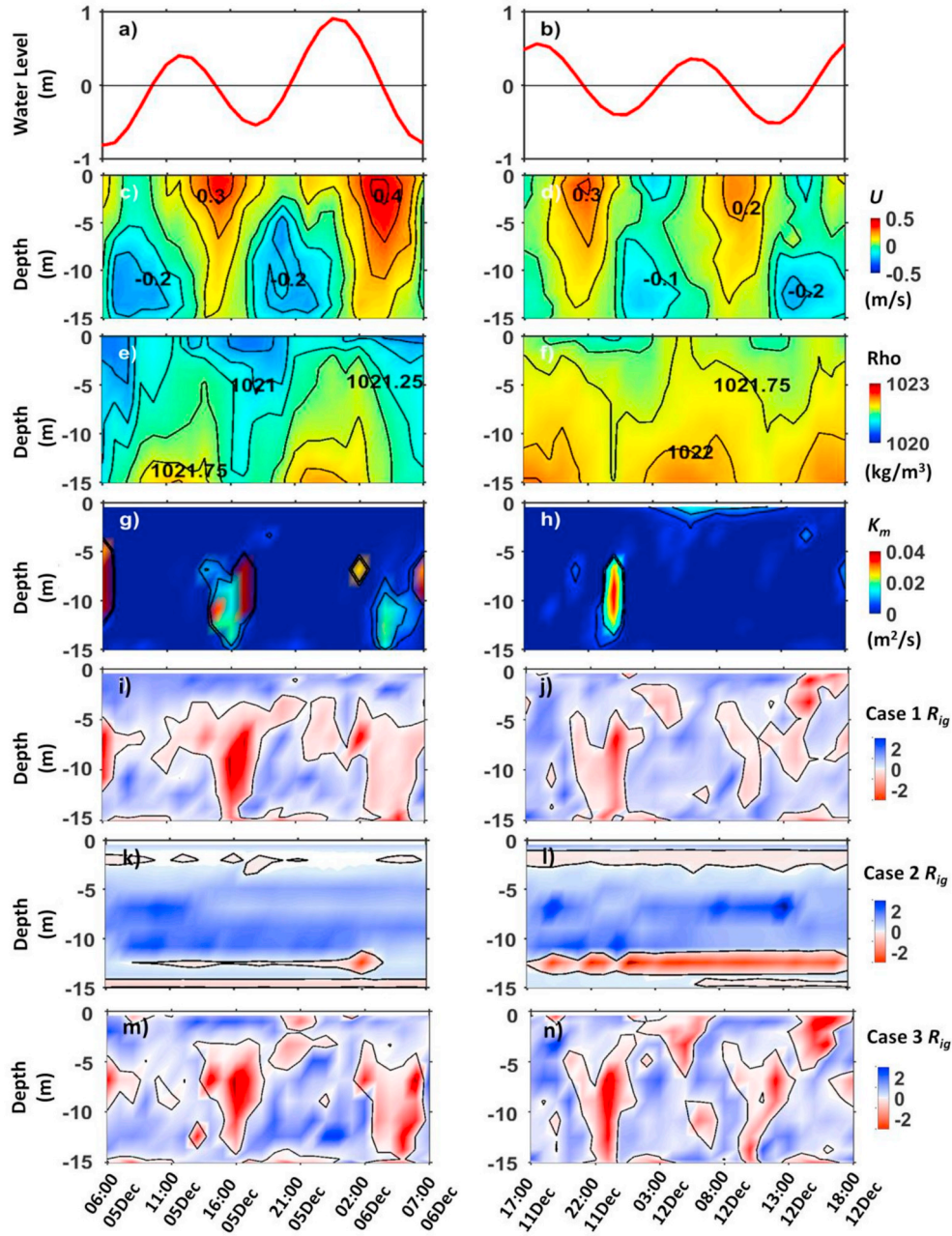
Fig. 8. Vertical and temporal variations in the estuary conditions at the GI station during spring (left column) and neap (right column): (a, b) sea surface elevation (m); (c, d) along-estuary current velocity profile (m/s); (e, f) density (kg/m³); (g, h) vertical eddy viscosity K_m (m²/s); (i, j) normalized R_{ig} in the Case 1 model forced by tide and low river flow; (k, l) normalized R_{ig} in the Case 2 model forced by low river flow only; (m, n) normalized R_{ig} in the Case 3 model forced by tides, low river flow and surface winds. The solid black line indicates $R_{ig} = 0.25$.

longitudinal circulation (Becherer et al., 2015). To explain how lateral circulation could generate a longitudinal circulation, Becherer et al. (2015) derived the vorticity transport equation for longitudinal circulation, based on the momentum equation:

$$\partial_t \omega_y = -\omega_x \omega_z - v\partial_y \omega_y - \omega_y \partial_z w - w\partial_z \omega_y - f\omega_x - \frac{1}{R_s}(v\omega_y - u\omega_x) - \partial_x b$$

$$- \partial_z(\partial_z < u'w'>) \tag{4}$$

This explained how the lateral circulation could generate a longitudinal circulation due to lateral bathymetry variability ($-\omega_x \omega_z$), Coriolis deflection ($-f\omega_x$) and curvature deflection ($-\frac{1}{R_s}(v\omega_y - u\omega_x)$) (from Eq. (4)). In SHE, the lateral bathymetry variability term played a more dominant role in determining ω_y than the other two mechanisms (Fig. 10b). During flood, the anti-clockwise lateral circulation yielded a

negative ω_x and the lateral gradient of the along-estuary velocity u yielded a positive ω_z, whereas the ebb tide lateral circulation generated a positive ω_x and negative ω_z. Since ω_x and ω_z had opposite orientation during flood and ebb at GI station (Fig. 10a), they increase ω_y, and contribute to the classical estuarine circulation during both flood and ebb (reduced flood current and increased ebb current). As $-\omega_x \omega_z$ made a larger contribution to the estuarine circulation during ebb, there was an increased ebb current compared to the flood current. In summary, results from the vorticity analysis in SHE demonstrate that the lateral variation in cross-channel bathymetry at near GI, generates a lateral circulation which amplifies intratidal asymmetry in along-estuary circulation.
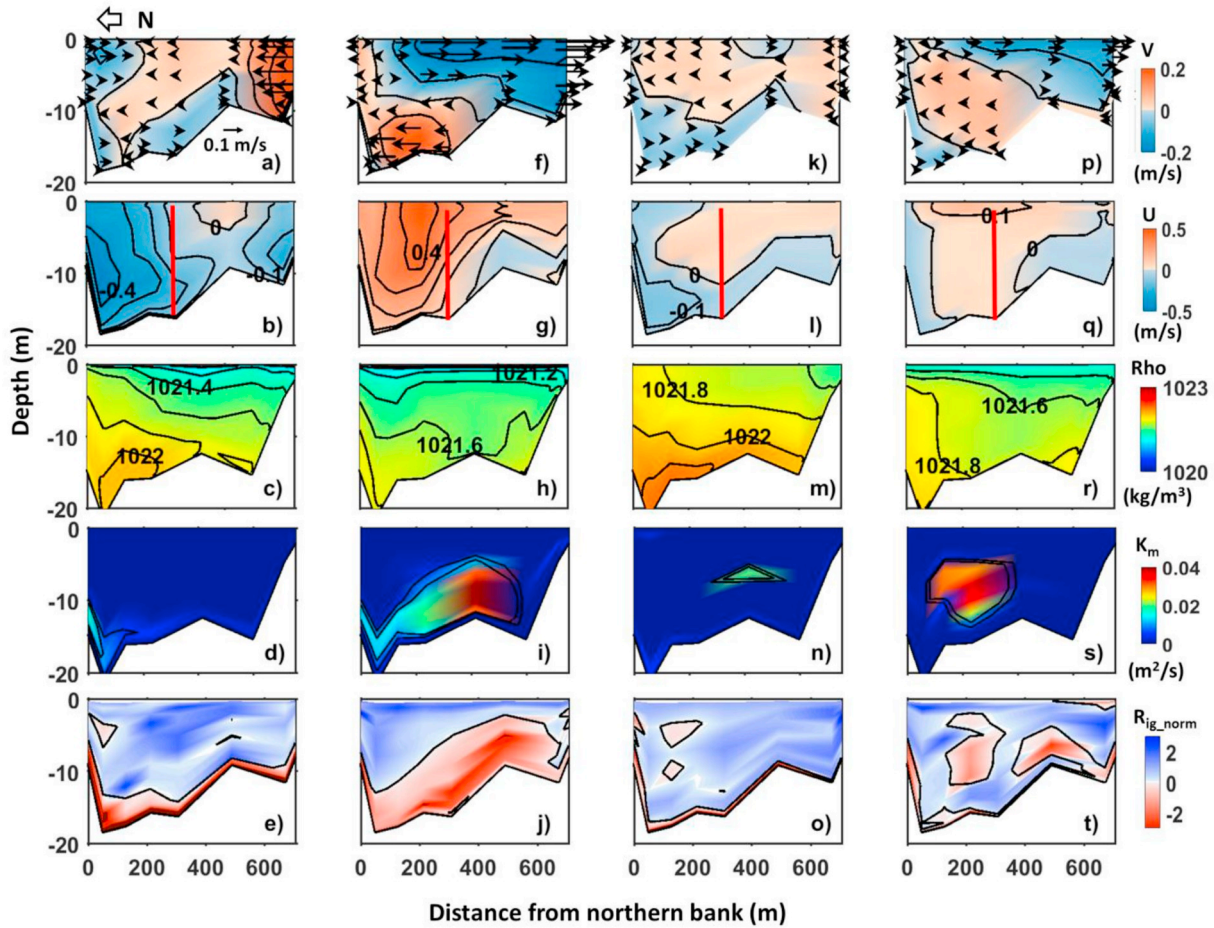
Fig. 9. Simulated temporal variations in the: lateral circulation v (m/s, row 1); along-channel advection u with ADCP profiler labelled as red line (m/s, row 2); density (kg/m³, row 3); vertical eddy viscosity K_m (m²/s, row 4); and normalized R_{ig} in Case 1 (row 5) along the section crossing the ADCP and CTD mooring station (Fig. 1). Columns 1 and 2 are spring flood and ebb tides, respectively, Columns 3 and 4 neap flood and ebb tides. (For interpretation of the references to colour in this figure legend, the reader is referred to the Web version of this article.)

4.4. Radius of curvature

At our study site, the channel curve was characterized by complex bending due to headlands, and modified by a small island in the main channel. The radius of curvature R_s, calculated using the method in Chant and Wilson (1997), was positive in the flow direction through a right-hand bend. Instead of two radii of curvature, for the flood and ebb counterturning bends, both the headlands and island channelled the flows, yielding multiple R_s along the cross-section during each tidal phase. Fig. 11 shows the different bends schematically (white arrows) between the headlands and island during flood and ebb. The depth-averaged relative vorticity ω_z showed a pattern of horizontal circulation during spring flood and ebb tide; a positive ω_z indicates anti-clockwise circulation (corresponding to a negative R_s) and a negative ω_z clockwise circulation (corresponding to a positive R_s) (Fig. 11). During flood, flows in the northern pathway were divided into a right-hand bend at the northern headland and a left-hand bend at the northern part of the island. Near the southern bank, flows bypassed the island in a right-hand bend and the southern headland in a left-hand bend (Fig. 11a). Currents were weaker over the shallow water, so that centrifugal force was stronger in the deep northern channel. During ebb tide, the streamlines adjusted accordingly between the headlands and the island (Fig. 11b). The radius of curvature was calculated as $\sim \pm 300$ m near the island and $\sim \pm 500$ m near the northern and southern headlands, with the signs corresponding to its circulation orientation.

4.5. Lateral-momentum budget

To investigate the generating mechanisms for the lateral circulation and its asymmetries, we employed the method described in Kalkwijk and Booij (1986). From their work, Eq. (5) describes the convection of lateral momentum influenced by the effect of curvature.

$$\frac{\partial v}{\partial t} = -\left(u\frac{\partial v}{\partial x} - \overline{u\frac{\partial v}{\partial x}}\right) + \frac{u^2 - \overline{u^2}}{Rs} - \frac{g}{\rho_o}\left(\int_z^0 \frac{\partial \rho(z')}{\partial y}dz' - \overline{\int_z^0 \frac{\partial \rho(z')}{\partial y}dz'}\right)$$
$$+ \left(K_m V_{zz} - \overline{K_m V_{zz}}\right). \tag{5}$$

The term on the left is the local acceleration of the lateral flow. The terms on the right are: advection in the along-estuary, the centrifugal force, the lateral baroclinic pressure gradient, and the vertical frictional dissipation. Since $u \gg v, w$, the advection of the lateral momentum in the cross-estuary direction and in the vertical direction were omitted. The magnitude of the Coriolis force was much weaker than other major forces and was also omitted.

The terms in Eq. (5) along the cross-channel section were calculated from model, and the intratidal variability in the major terms at GI station during spring and neap tides are shown in Fig. 12. Vertical variations in the major momentum terms at GI station during flood and ebb in the spring and neap tides (same time period as Fig. 9) are plotted in Fig. 13. The analysis was focused on GI station located in the thalweg, where most of the momentum was captured and the strongest baroclinic pressure gradient was preserved. During spring flood tide,
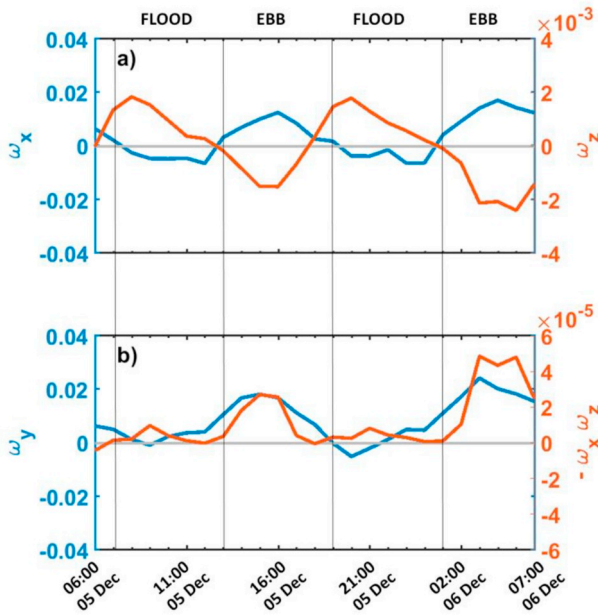
Fig. 10. (a) Simulated depth-averaged along-estuary vorticity ω_x (blue) and relative vorticity ω_z (red) at GI station during spring tide; (b) redistribution of the along-estuary momentum due to lateral circulation $- \omega_x \omega_z$ (red) and the depth-averaged cross-estuary vorticity ω_y (blue) at GI station during spring tide. (For interpretation of the references to colour in this figure legend, the reader is referred to the Web version of this article.)

the lateral baroclinic pressure gradient predominantly drove anti-clockwise lateral circulations (Fig. 12c). The streamlines were curved by the island, and currents deflected towards the north at the surface with backflow towards the south at depth under the barotropic pressure gradient, reinforcing the differential-advection-induced lateral circulation (Fig. 12d). During spring ebb tide, currents were mainly deflected by the northern headland, and the centrifugal force had opposite directions in the water column, southward at the surface and northward at the bottom (Fig. 12d). Stronger ebb currents redistributed the density field across the channel (Fig. 9h), leading to a weakened lateral baroclinic pressure gradient (Figs. 12c and 13b). The centrifugal force was stronger during ebb, as it is highly correlated to the strength of the along-channel velocity u, which was relatively weak during flood and strong during ebb (Fig. 8c). The non-linear advective term $- \left(u \frac{\partial v}{\partial x} - \overline{u \frac{\partial v}{\partial x}} \right)$, which is the adjustment of the streamline, also closely related to u, became the dominant force driving the lateral circulation during ebb (Figs. 12b and 13b). Friction was found to counteract the bottom motion across the channel, with an increased magnitude during ebb because of the stronger lateral current (Fig. 12e).

During neap tides, weakened current impacted on the strength of the major momentum terms without shutting down lateral circulation, and resulted in a more complex structure (Fig. 9p). Compared with spring tides, centrifugal force was reduced corresponded to weakened along-estuary velocity (Fig. 12k) and the lateral baroclinic pressure gradient became important (Fig. 12j). The advective term remained relatively strong (Fig. 12i), with the same orientation as during spring tides. During neap flood, the differential-advection-induced baroclinic pressure gradient and the centrifugal force dominated lateral circulation throughout the water column, forming an anti-clockwise flow (Fig. 9k). During neap ebb, the non-linear advective term and the centrifugal force drove southward flow at the surface, as surface currents were strong, then were quickly overcome by the baroclinic pressure gradient below the surface layer driving an anti-clockwise circulation at the sub-surface. Such a three-layer flow structure was also observed by Nidzieko et al. (2009) during stratified ebb over neap tides.

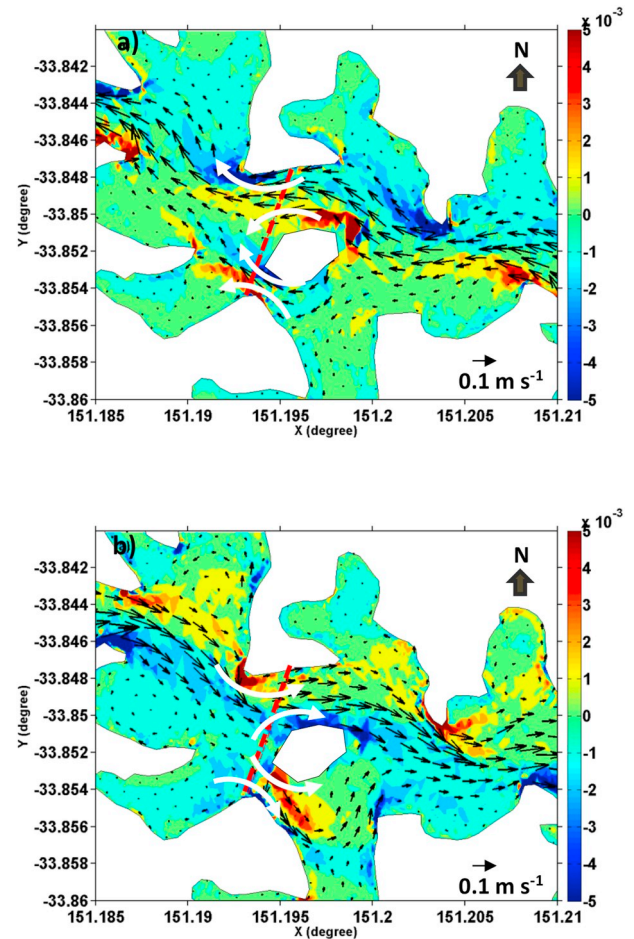From Fig. 8, both the eddy viscosity and normalized R_{ig} indicate the

Fig. 11. Depth-averaged relative vorticity ω_z during (a) flood and (b) ebb during the spring tide. Positive values (red) indicate anti-clockwise circulation, negative values (blue) clockwise circulation in the horizontal plane. The cross-section is shown by the red dashed line. Flow paths along the curved channels are shown by the white arrows, the along-estuary flood/ebb current by the black arrows. (For interpretation of the references to colour in this figure legend, the reader is referred to the Web version of this article.)

development of intratidal asymmetries of vertical mixing. The scaled F_r is plotted against the bulk internal F_r in Fig. 12a and h, using Eq. (2) and Eq. (3). F_r, scaled by the curvature effect (blue line), indicated the curvature-induced lateral circulation should have been strong enough to overturn the density field at each tidal stage according to Seim and Gregg (1997). However, the bulk internal F_r (red line) only exceeded the overturning threshold during ebb tides. This indicates that the occurrence of density overturning also depends on the along-estuary current velocity. Using Eq. (2), setting $F_r^2 = 1$ and using the vertical density gradient up to $0.25 \, kg/m^2$ during spring and $0.07 \, kg/m^2$ during neap at a total water depth of 18 m, gave a depth-averaged along-estuary velocity, $\bar{u}$ between $\pm 0.2 \, m/s$ during spring tide and $\pm 0.1 \, m/s$ during neap tide, when the buoyancy force was strong enough to stabilize the water column and suppress lateral circulation due to shear instabilities. The maximum observed depth-averaged along-estuary currents during spring and neap (Fig. 5c and d). suggested the ebb currents over spring and neap were sufficient to overcome vertical stratification and mix the water column, while stratification was preserved during flood because of the along-estuary current being weak.

Overall during stratified flood over spring tides, the centrifugal force was weak, limited by the relatively low along-estuary current. The differential-advection-induced baroclinic pressure gradient became dominant, and produced lateral circulation with the same sense of rotation as the curvature. The baroclinic pressure gradient and centrifugal
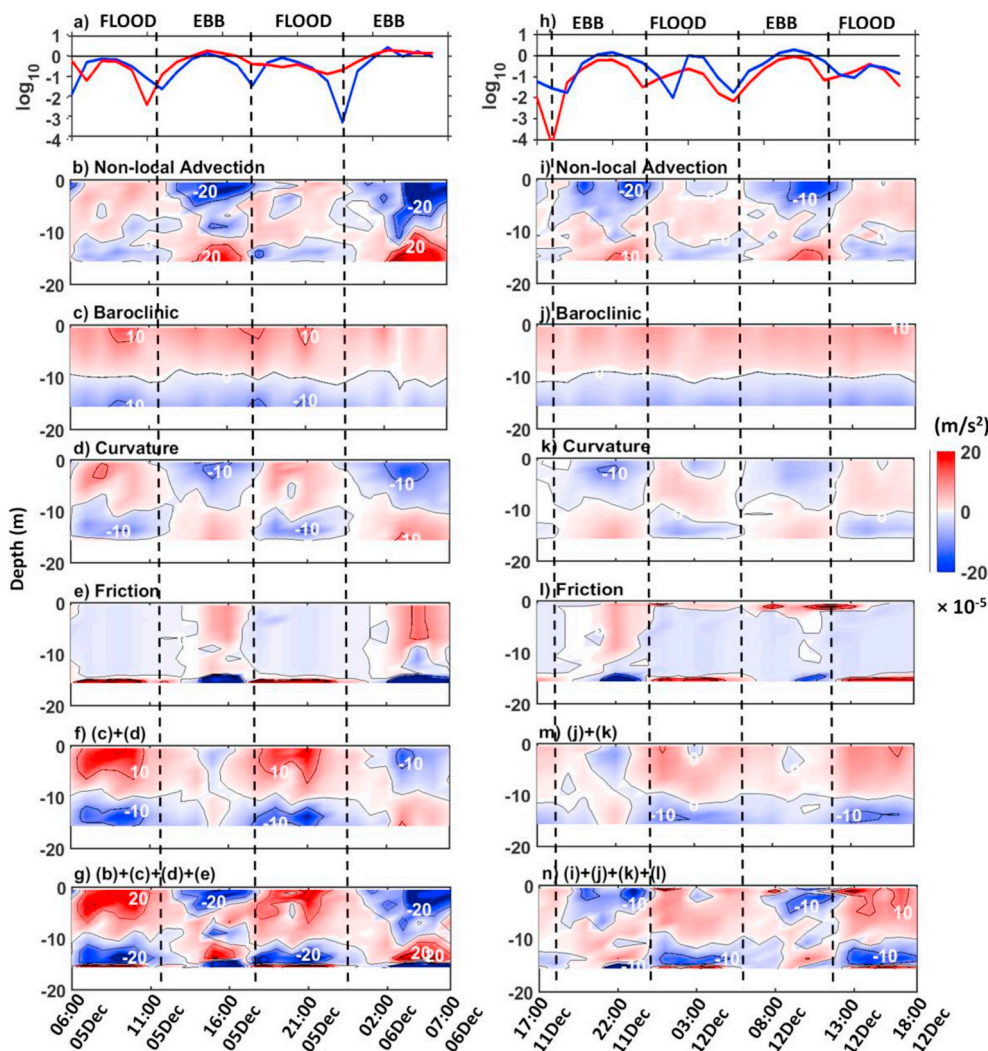
Fig. 12. Times series at GI station during spring tides (left) and neap tides (right): (a, h) bulk internal Froude number (Eq. (2), red line) and surface internal Froude number scaled by curvature (Eq. (3), blue line); (b - e, i - l) vertical deviation from depth-averaged terms in lateral momentum Eq. (5) in m/s^2 × 10^{-5}; (f, m) sum of baroclinic pressure gradient and centrifugal force; (g, n) sum of non-local advection, baroclinic pressure gradient, centrifugal force and friction. (For interpretation of the references to colour in this figure legend, the reader is referred to the Web version of this article.)

force worked in concert throughout the water column to drive anti-clockwise lateral circulation. During mixed ebb over spring tides, the stronger centrifugal force worked in concert with the non-linear advective term establishing a classic two-layer helical flow. The clockwise lateral circulation was strong enough to break down the stratification, and was transferred into the along-estuary circulation according to Eq. (4). During stratified ebb over neap tides, a weaker centrifugal force and non-linear advection together with a relatively stronger lateral baroclinic pressure gradient generated a three-layer flow. The lateral flow profile was consistent with a density-driven flow, though curvature effects remained at the surface layer. The intratidal asymmetry in the lateral flow, with stronger magnitude during ebb than flood, was mainly attributed to the asymmetric centrifugal force and the advective term corresponding to the along-estuary current asymmetries.

4.6. Lateral-momentum analysis over the whole estuary

The numerical model allows the application of a lateral-momentum analysis over the whole estuary during the different tidal stages. The dominant forcing driving the lateral circulations during quiescent conditions was determined at six cross-sections, selected from the estuary head towards the estuary mouth to represent different sections of

the estuary. Absolute values of the variations in the major momentum terms were sectional-averaged across each section during flood and ebb in the spring; the percentage contributions of each term at these sections, XS1-XS6, are plotted in the pie charts in Fig. 14. Friction contributes 51–60% during both flood and ebb in the spring at the estuary head (XS1), where the water is very shallow (< 2 m). At the estuary mouth (XS6), where the along-estuary current is strong, non-linear advection makes the greatest contribution (51–60%). Due to the complex channel geometry in the upper and lower estuary (XS2-XS5), non-linear advection has a constant large influence (20–40%) on generating lateral circulations by transferring the along-estuary momentum to the lateral momentum. The curvature effect makes a significant contribution (up to 48%) at the sections with channel bends, with greater influence during ebb than flood due to the stronger ebb currents. The lateral baroclinic pressure gradient becomes more important at XS5, where both curvature effects and non-linear advection are less significant.

During neap tide (figure not shown here), the lateral baroclinic pressure gradient is the dominant force generating the lateral circulations along the estuary during both flood and ebb. The ultimate orientation of the lateral circulation is the result of the combined effects of the lateral baroclinic pressure gradient, the curvature effect and non-
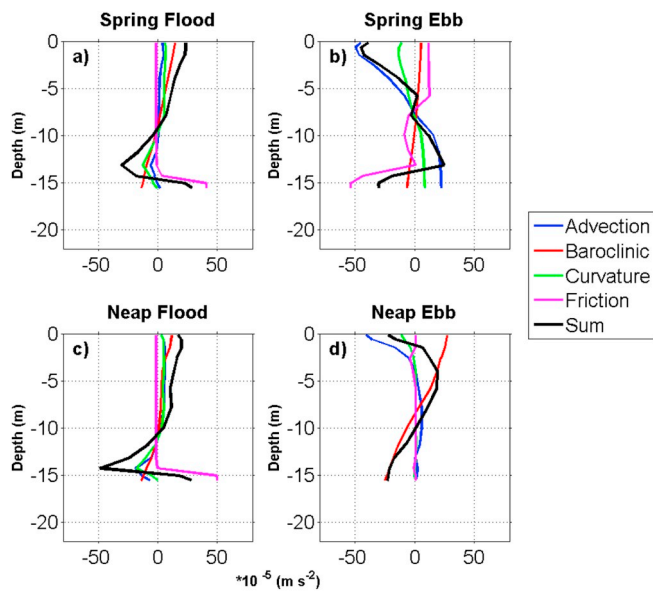
Fig. 13. Vertical profile of the major momentum terms in Eq. (5) at GI station during flood and ebb in the spring and neap tides.
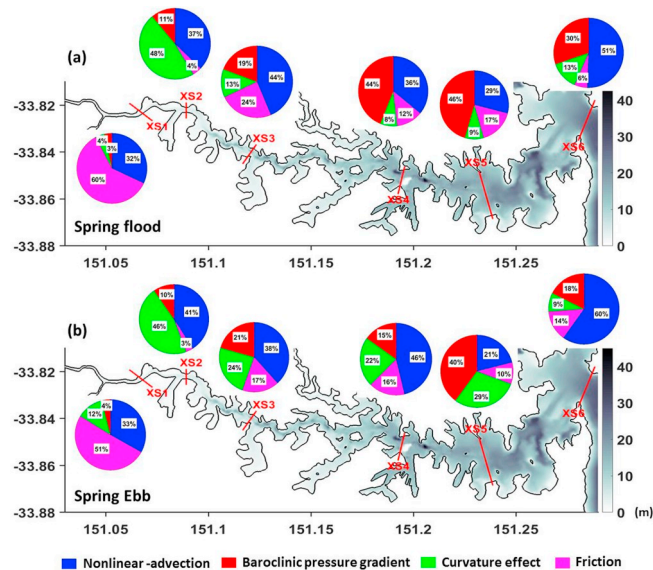

Fig. 14. Contribution (%) of each forcing in the cross-section averaged lateral-momentum equation at cross-sections XS1-XS6, from the estuary head (XS1) towards the estuary mouth (XS6): (a) spring flood; (b) spring ebb. Red lines indicate the respective cross-sections. (For interpretation of the references to colour in this figure legend, the reader is referred to the Web version of this article.)

linear advection.

5. Conclusions

Monitoring and modelling of the Sydney Harbour Estuary during low-flow periods revealed intratidal interactions between tides, irregular channel shape, and variable bathymetry, produces asymmetries in lateral circulation and vertical mixing. Lateral processes in turn influence along-estuary circulation. Variations in intra- and intertidal vertical mixing highlights that, rather than being in a tidally averaged steady state, Sydney Harbour Estuary is in a continual state of adjustment to variations in the forcing conditions. Down-estuary and up-estuary winds enhance stratification and mixing processes of the system, respectively, however do not generate lateral circulation and intratidal asymmetries.

Lateral motions in this estuary are controlled by lateral baroclinic pressure gradients, centrifugal force and non-linear advection. During flood tide the centrifugal force and baroclinic pressure gradient cause stratified flow. When the along-estuary circulation is strong, channel bends produce lateral circulation as a classic helical flow which is able to overcome stratification and produce a well-mixed water column. This mixing behaviour is most evident during spring ebb tides. The strength of the lateral circulation in Sydney Harbour Estuary is weakened by stratification, and a three-layer circulation structure is generated by a depth-varying balance between curvature effect and baroclinic pressure gradient during neap ebb.

Numerical modelling of the Sydney Harbour Estuary revealed that the highly variable cross-channel bathymetry is the major driver of intratidal asymmetries in along-estuary circulation. Model simulations also confirmed the effect of channel bends on the interaction between lateral and along-estuary circulation as well as vertical mixing in the estuary. Lateral circulation redistributes lateral shear in along-estuary momentum and influences on the classical estuarine circulation. The stronger flow during ebb tides results in stronger curvature effects and non-linear advection, which in turn leads to intra-tidal asymmetries in lateral circulation and vertical mixing. In a rotating and narrow channel, lateral circulation responses quicker to local topographic effect than external forcing (e.g. wind forcing), thus wind forcing does not necessarily contribute to lateral circulation in a sinuous channel. However wind forcing can introduce additional straining or mixing effects on the system. These findings highlight the important role estuarine geometry plays in lateral and longitudinal circulation, which can be widely applied in other estuaries with sinuous channel and variable bathymetry. The study presents a detailed investigation of an estuarine system unlike typical Strain Induced Periodic Stratification (SIPS) proposed by Simpson et al. (1990), enhancing understanding of the processes that govern circulation in complex waterways.

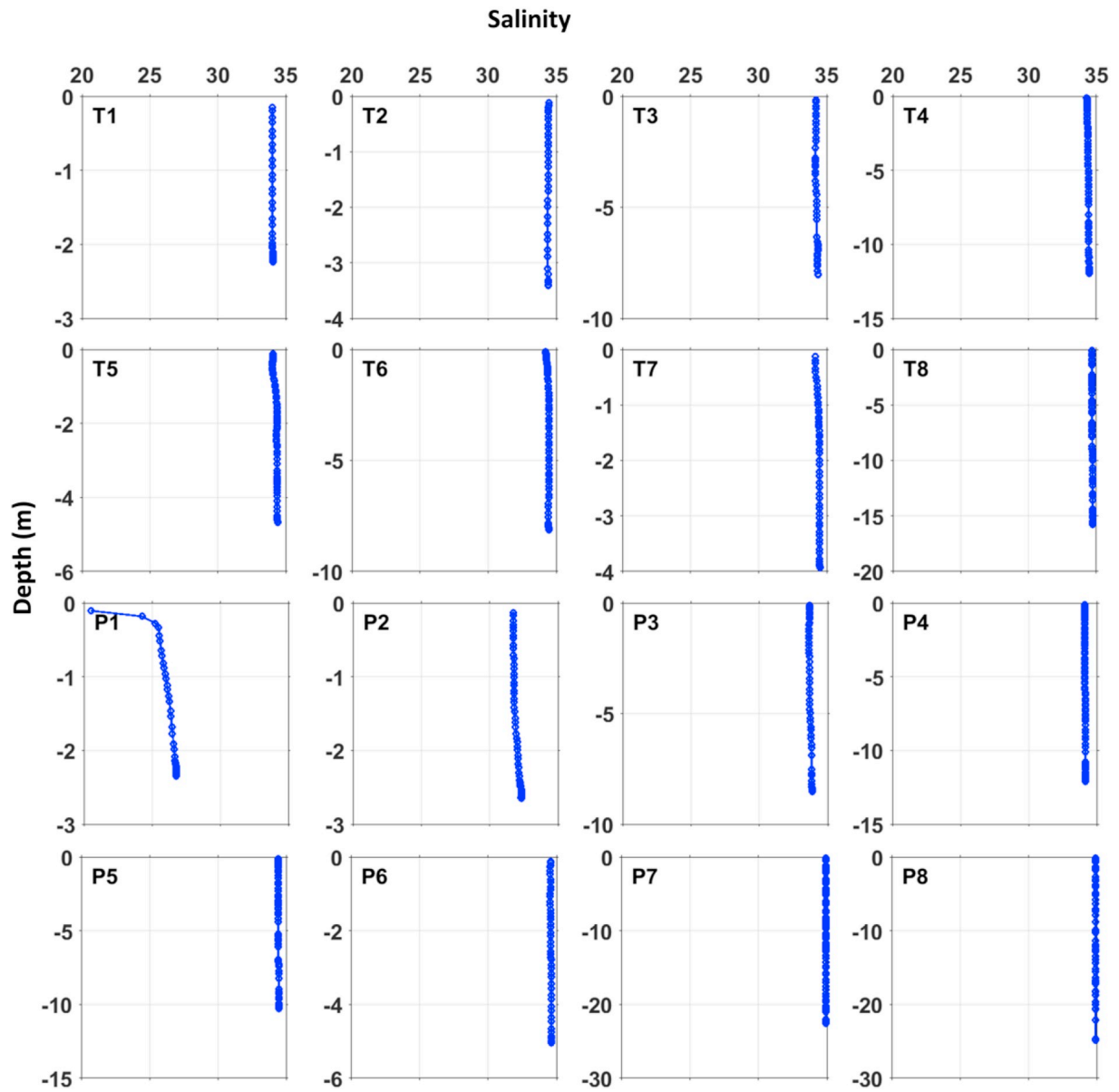## Appendix A. Measured CTD data for model setup and calibration

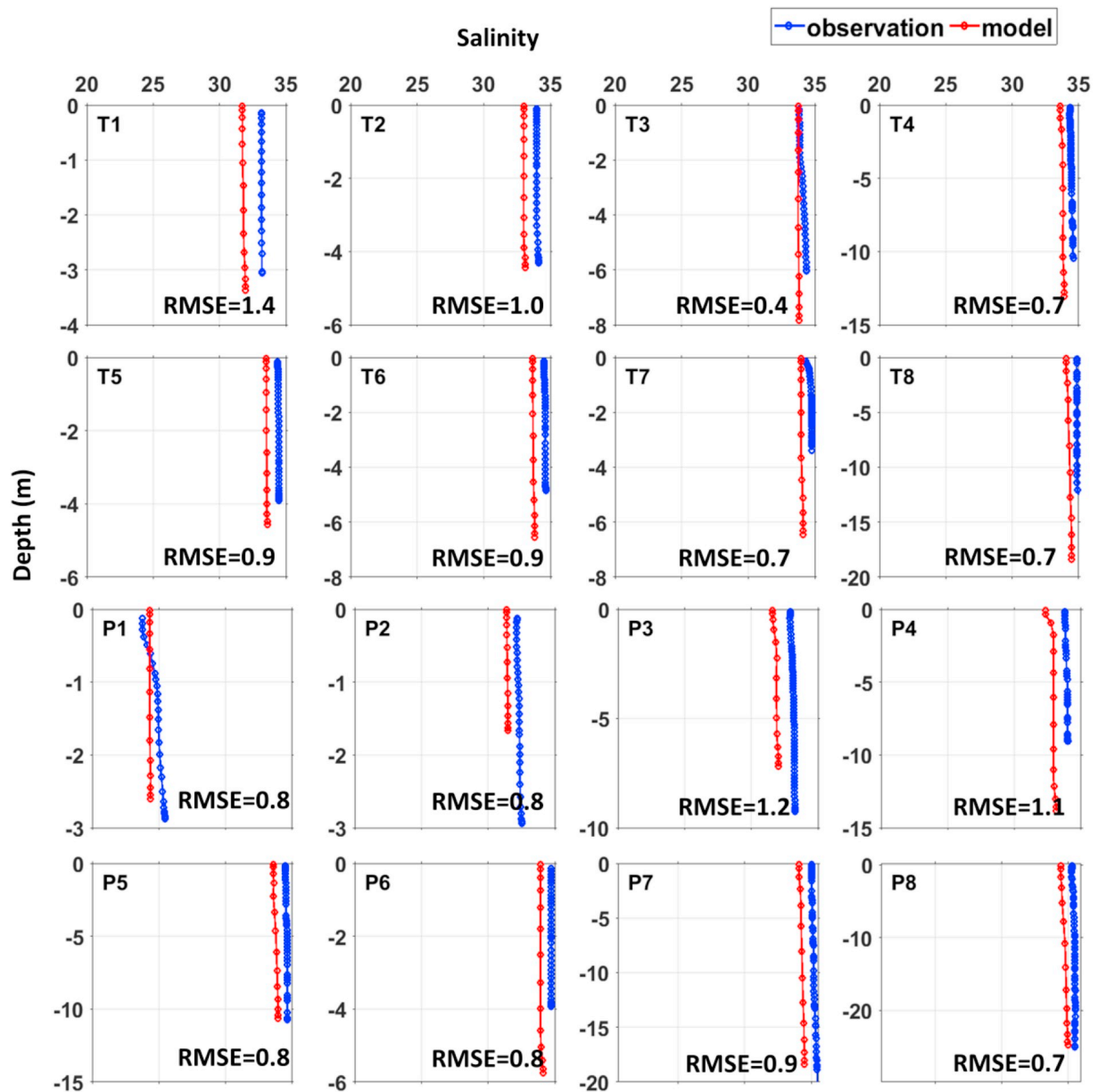**Fig. A-1.** Salinity profiles measured on 15th Oct 2013 for estuarine initial salinity field setup.

Fig. A-2. Salinity profiles measured on 18th December 2013 during low-runoff conditions for model calibration.

References

Becherer, J., Stacey, M.T., Umlauf, L., Burchard, H., 2015. Lateral circulation generates flood tide stratification and estuarine exchange flow in a curved tidal inlet. J. Phys. Oceanogr. 45 (3), 638–656. https://doi.org/10.1175/jpo-d-14-0001.1.

Birch, G.F., Rochford, L., 2010. Stormwater metal loading to a well-mixed/stratified estuary (Sydney Estuary, Australia) and management implications. Environ. Monit. Assess. 169 (1–4), 531–551. https://doi.org/10.1007/s10661-009-1195-z.

Blanckaert, K., de Vriend, H.J., 2005. Turbulence characteristics in sharp open-channel bends. Phys. Fluids 17 (5), 055102. https://doi.org/10.1063/1.1886726.

Blanckaert, K., De Vriend, H.J., 2005b. Turbulence structure in sharp open-channel bends. J. Fluid Mech. 536, 27–48. https://doi.org/10.1017/s0022112005004787.

Buijsman, M.C., Ridderinkhof, H., 2008. Variability of secondary currents in a weakly stratified tidal inlet with low curvature. Continent. Shelf Res. 28 (14), 1711–1723. https://doi.org/10.1016/j.csr.2008.04.001.

Chant, R.J., Wilson, R.E., 1997. Secondary circulation in a highly stratified estuary. J. Geophys. Res.: Oceans 102 (C10), 23207–23215. https://doi.org/10.1029/97jc00685.

Chant, R.J., 2002. Secondary circulation in a region of flow curvature: relationship with tidal forcing and river discharge. J. Geophys. Res. 107 (C9). https://doi.org/10.1029/2001jc001082.

Chen, C., Liu, H., Beardsley, R.C., 2003. An unstructured grid, finite-volume, three-dimensional, primitive equations ocean model: application to coastal ocean and estuaries. J. Atmos. Ocean. Technol. 20 (1), 159–186. https://doi.org/10.1175/1520-0426(2003)020<0159:AUGFVT>2.0.CO;2.

Chen, S.-N., Sanford, L.P., 2009. Lateral circulation driven by boundary mixing and the associated transport of sediments in idealized partially mixed estuaries. Continent. Shelf Res. 29 (1), 101–118. https://doi.org/10.1016/j.csr.2008.01.001.

Cheng, P., Wilson, R.E., Chant, R.J., Fugate, D.C., Flood, R.D., 2009. Modeling influence of stratification on lateral circulation in a stratified estuary. J. Phys. Oceanogr. 39 (9), 2324–2337. https://doi.org/10.1175/2009jpo4157.1.

Collignon, A.G., Stacey, M.T., 2012. Intratidal dynamics of fronts and lateral circulation at the shoal-channel interface in a partially stratified estuary. J. Phys. Oceanogr. 42 (5), 869–883. https://doi.org/10.1175/jpo-d-11-065.1.

Das, P., Marchesiello, P., Middleton, J.H., 2000. Numerical modelling of tide-induced residual circulation in Sydney Harbour. Mar. Freshw. Res. 51 (2), 97–112. https://doi.org/10.1071/MF97177.

Ferziger, J.H., Koseff, J.R., Monismith, S.G., 2002. Numerical simulation of geophysical turbulence. Comput. Fluids 31, 557–568.

Hatje, V., Birch, G.F., Hill, D.M., 2001. Spatial and temporal variability of particulate trace metals in Port Jackson Estuary, Australia. Estuarine. Coastal and Shelf Science 53 (1), 63–77. https://doi.org/10.1006/ecss.2001.0792.

Howard, L., 1961. Note on a paper of John W. Miles. J. Fluid Mech. 10 (4), 509–512. https://doi.org/10.1017/S0022112061000317.

Huijts, K.M.H., Schuttelaars, H.M., de Swart, H.E., Friedrichs, C.T., 2009. Analytical study of the transverse distribution of along-channel and transverse residual flows in tidal estuaries. Continent. Shelf Res. 29 (1), 89–100. https://doi.org/10.1016/j.csr.2007.

09.007.

Kalkwijk, J.P.T., Booij, R., 1986. Adaptation of secondary flow in nearly-horizontal flow. J. Hydraul. Res. 24 (1), 19–37. https://doi.org/10.1080/00221688609499330.

Kim, Y.H., Voulgaris, G., 2008. Lateral circulation and suspended sediment transport in a curved estuarine channel: Winyah Bay, SC, USA. J. Geophys. Res. 113 (C9). https://doi.org/10.1029/2007jc004509.

Lacy, J.R., Monismith, S.G., 2001. Secondary currents in a curved, stratified, estuarine channel. J. Geophys. Res.: Oceans 106 (C12), 31283–31302. https://doi.org/10.1029/2000jc000606.

Lacy, J.R., 2003. Interaction of lateral baroclinic forcing and turbulence in an estuary. J. Geophys. Res. 108 (C3). https://doi.org/10.1029/2002jc001392.

Lee, S.B., Birch, G.F., 2012. Utilising monitoring and modelling of estuarine environments to investigate catchment conditions responsible for stratification events in a typically well-mixed urbanised estuary. Estuar. Coast Shelf Sci. 111, 1–16. https://doi.org/10.1016/j.ecss.2012.05.034.

Lee, S.B., Birch, G.F., Lemckert, C.J., 2011. Field and modelling investigations of fresh-water plume behaviour in response to infrequent high-precipitation events, Sydney Estuary, Australia. Estuar. Coast Shelf Sci. 92 (3), 389–402. https://doi.org/10.1016/j.ecss.2011.01.013.

Lerczak, J., Geyer, W., 2004. Modeling the lateral circulation in straight, stratified estuaries. J. Phys. Oceanogr. 34, 1410–1428. https://doi.org/10.1175/15200485(2004)034,1410:MTLCIS.2.0.CO;2.

Li, C., O'Donnell, J., 1997. Tidally driven residual circulation in shallow estuaries with lateral depth variation. J. Geophys. Res.: Oceans 102 (C13), 27915–27929. https://doi.org/10.1029/97jc02330.

Li, M., Cheng, P., Chant, R., Valle-Levinson, A., Arnott, K., 2014. Analysis of vortex dynamics of lateral circulation in a straight tidal estuary. J. Phys. Oceanogr. 44 (10), 2779–2795. https://doi.org/10.1175/jpo-d-13-0212.1.

Li, Y., Li, M., 2012. Wind-driven lateral circulation in a stratified estuary and its effects on the along-channel flow. J. Geophys. Res.: Oceans 117 (C9). https://doi.org/10.1029/2011jc007829.

Mellor, G.L., Yamada, T., 1982. Development of a turbulence closure model for geophysical fluid problems. Rev. Geophys. 20 (4), 851–875. https://doi.org/10.1029/RG020i004p00851.

Miles, J., 1961. On the stability of heterogeneous shear flows. J. Fluid Mech. 10 (4),

496–508. https://doi.org/10.1017/S0022112061000305.

Nidzieko, N.J., Hench, J.L., Monismith, S.G., 2009. Lateral circulation in well-mixed and stratified estuarine flows with curvature. J. Phys. Oceanogr. 39 (4), 831–851. https://doi.org/10.1175/2008jpo4017.1.

Nunes, R., Simpson, J., 1985. Axial convergence in a well-mixed estuary. Estuar. Coast Shelf Sci. 20, 637–649. https://doi.org/10.1016/0272-7714(85)90112-X.

Ott, M.W., Dewey, R., Garrett, C., 2002. Reynolds stresses and secondary circulation in a stratified rotating shear flow. J. Phys. Oceanogr. 32, 3249–3268.

Pawlowicz, R., Beardsley, B., Lentz, S., 2002. Classical tidal harmonic analysis including error estimates in MATLAB using T_TIDE. Comput. Geosci. 28 (8), 929–937. https://doi.org/10.1016/S0098-3004(02)00013-4.

Pein, J., Valle-Levinson, A., Stanev, E.V., 2018. Secondary circulation asymmetry in a meandering, partially stratified estuary. J. Geophys. Res.: Oceans. https://doi.org/10.1002/2016JC012623. (in press).

Roy, P., 1983. Quaternary geology. In: Herbert, C. (Ed.), Geology of the Sydney 1;100,000 Sheet. Publ. Geological Survey of NSW, Dept. of Mineral Resources, Sydney, Australia.

Scully, M.E., Friedrichs, C., Brubaker, J., 2005. Control of estuarine stratification and mixing by wind-induced straining of the estuarine density field. Estuaries 28, 321–326. https://doi.org/10.1007/BF02693915.

Seim, H.E., Gregg, M.C., 1997. The importance of aspiration and channel curvature in producing strong vertical mixing over a sill. J. Geophys. Res. 102, 3451–3472.

Simpson, J.H., Brown, J., Matthews, J., Allen, G., 1990. Estuaries 13, 125. https://doi.org/10.2307/1351581.

Smagorinsky, J., 1963. General circulation experiments with the primitive equations. Mon. Weather Rev. 91 (3), 99–164. https://doi.org/10.1175/1520-0493(1963)091<0099:GCEWTP>2.3.CO;2.

Smith, R., 1976. Longitudinal dispersion of a buoyant contaminant in a shallow channel. J. Fluid Mech. 78 (4), 677–688. https://doi.org/10.1017/S0022112076002681.

Stacey, M.T., Fram, J.P., Chow, F.K., 2008. Role of tidally periodic density stratification in the creation of estuarine subtidal circulation. J. Geophys. Res. 113 (C8). https://doi.org/10.1029/2007jc004581.

Williamson, N., Norris, S.E., Armfield, S.W., Kirkpatrick, M.P., 2012. Lateral circulation in a stratified open channel on a 120° bend. Water Resour. Res. 48 (12). https://doi.org/10.1029/2012wr012218.